**PAPER • OPEN ACCESS**

# Species-dependent tunneling ionization of weakly bound atoms in the short-wave infrared regime

View the article online for updates and enhancements.

# New Journal of Physics

The open access journal at the forefront of physics

CrossMark

**PAPER**

# Species-dependent tunneling ionization of weakly bound atoms in the short-wave infrared regime

D Zille[1,2], D Adolph[1,2], S Skruszewicz[1,2], A M Sayler[1,2] and G G Paulus[1,2]

1   Institute of Optics and Quantum Electronics, Friedrich Schiller University Jena, Max-Wien-Platz 1, 07743 Jena, Germany
2   Helmholtz Institut Jena, Fröbelstieg 3, 07743 Jena, Germany

## Abstract

We investigate the intensity- and species-dependent strong-field ionization of alkali metal atoms; sodium, potassium, rubidium and caesium; by intense, few-cycle laser pulses in the short-wave infrared (sw-IR) regime at 1800 nm. The low ionization potential, $I_p$, of these atoms allows us to scale the interaction and study the tunneling regime at sw-IR wavelengths using low intensities and pulse energies. Measurements of above-threshold ionization spectra in the alkali species exhibit distinct differences to rare gas spectra at 800 and 1800 nm. However, pairing the low ionization potential of these atoms with longer wavelengths results in the reemergence of some well-know features of nobel gas spectra in the visible, e.g., the plateau. Our focus lies on the comparison of high-energy rescattered electron yield among the different alkali species. The highly unfavorable plateau scaling known from rare gases at longer wavelengths is successfully circumvented by switching to low-$I_p$ targets. In the investigated parameter range, we identify potassium as the most efficient rescatterer. In addition, this paves the way to a carrier-envelope phasemeter operating in the sw-IR/mid-wave IR regime, employing alkali metal atoms as a target.

## 1. Introduction

During the ionization of an atom by a strong laser field, electrons can absorb more photons than are necessary for their liberation. This so-called above-threshold ionization (ATI) [1] is the prerequisite for many important effects, for example high-harmonic generation (HHG) or non-sequential double ionization [2, 3]. The dynamics underlying ATI are commonly divided into two regimes, characterized by the Keldysh parameter, $\gamma = \omega_0 \sqrt{2I_p/I}$ [4] (atomic units are used throughout, unless otherwise stated), where $\omega_0$ is the laser angular frequency, $I_p$ is the ionization potential of the atom, and $I$ is the laser intensity. Ionization occurs in the multiphoton regime if $\gamma > 1$, whereas $\gamma < 1$ is associated with the tunneling regime, in which the laser electric field distorts the Coulomb potential, allowing the electron to tunnel underneath the barrier.

So far, most studies of ATI, e.g., the discovery of the so-called plateau [5] or HHG with its important and far reaching applications, were performed around 800 nm using rare gases as target atoms. The main selection criteria for these atomic species are their ease of use and the existence of strongly bound valence electrons, i.e., their large ionization potential ($I_p \approx 12$ eV). This, in turn, allows for a relatively high laser intensity ($I \approx 10^{14}$ W cm$^{-2}$) before saturation occurs and the tunneling regime, $\gamma < 1$, can be reached. Similarly, higher harmonics of the fundamental can be generated. However, in recent years strong-field ionization at longer wavelengths in the sw-IR regime has drawn significant attention, mainly driven by the desire to push HHG to higher photon energies, which enabled the possibility of ever shorter, isolated attosecond pulses [6, 7].

Many of the promising applications of strong-field physics are based on a significant yield of rescattered electrons. Longer driving wavelengths decisively reduce the production of high-energy electrons. A highly unfavorable scaling of the plateau yield with the wavelength, $Y_{plateau} \propto \lambda^{-5.5\pm0.5}$, has been found [8]. The conversion efficiency of HHG could similarly be shown to behave as $\lambda^{-5}$ to $\lambda^{-6}$, or worse [9, 10].

Additionally, many modern lasers systems operating in the sw-IR/mid-wave IR (MIR) regime output relatively low pulse energies, especially for few-cycle pulses. The potential solution to reduce the intensity in experiments is usually not feasible as it would lead to impractically long measurement times and abandonment of the tunneling regime.

In this paper we circumvent these challenges by moving to a largely unexplored atomic species for strong-field ionization, the alkali metal atoms: sodium, potassium, rubidium and caesium. Their valence electron is only weakly bound ($I_p \approx$ 4–5 eV) allowing for a significant reduction in the required laser intensity. By increasing the wavelength and ionizing these low-$I_p$ targets at 1800 nm we keep the Keldysh parameter roughly unchanged with respect to the rare gases at the higher intensities and 800 nm. Through this concept of a scaled interaction [8], we remain in the tunneling regime and observe the formation of a plateau and significant yield of high-energy electrons. An additional advantage of alkali metal atoms is their genuine single-valence-electron character. This makes them perfect candidates to test and employ the well-known single active electron approximation. Finally, due to the low pulse energy required, they are perfectly suited to study the transition from multiphoton [11] to the tunneling and into the saturation regime for sw-IR/MIR wavelengths.

This simple scaling argument suggests a largely similar behavior of rare gases and alkali metal atoms at their respective saturation intensity. Surprisingly, we observe this not to be the case. The alkali ATI spectra show several characteristics, which can not yet be connected with the rare gases. This further supports that the investigation of low-$I_p$ targets can lead to unexpected effects as has recently been shown, e.g., diffractive imaging and suppression of the low-energy structure in $C_{60}$ [12, 13]; forward rescattering in silver clusters [14]; low-energy structure in rare gas clusters [15]; and steering of ultrafast electron pulses in metallic nanotips [16].

In general, some previous results on SFI of alkalis exist: employing ultracold rubidium atoms, absolute ionization probabilities could be measured and excellently compared with *ab initio* theory [17]. Angular distributions of lithium at 785 nm in the over-the-barrier regime were reported in reference [18]. These results could be shown to be significantly influenced by the creation of Rydberg states from the leading edge of the pulse [19]. A study of the resonance-enhanced four-photon ionization of lithium was shown in reference [20]. The importance of Rydberg states in SFI of alkalis was again addressed by demonstrating selective excitation and attenuation of high-lying states in sodium. In a different regime, Gallagher has extensively studied alkali Rydberg atoms [21] exposed to microwave radiation, e.g., population transfer in sodium [22], or dipole–dipole broadening in rubidium [23].

Specifically, we study the intensity-dependent yield of plateau electrons among the different alkali targets. A strong species dependence is observed [24]. The of this dependence is found to be a direct consequence of the differential scattering cross-sections due to the different atomic potentials. This investigation further paves the way to the construction of a device, which can measure the CEP of single laser shots based on rescattered electrons, e.g., the so-called carrier-envelope phasemeter (CEPM) [25], in the sw-IR/MIR regime. At 800 nm the CEPM operates with xenon as a target gas, but due to the unfavorable scaling mentioned above, the extension to longer wavelengths necessitates the usage of a low-$I_p$ target [26].
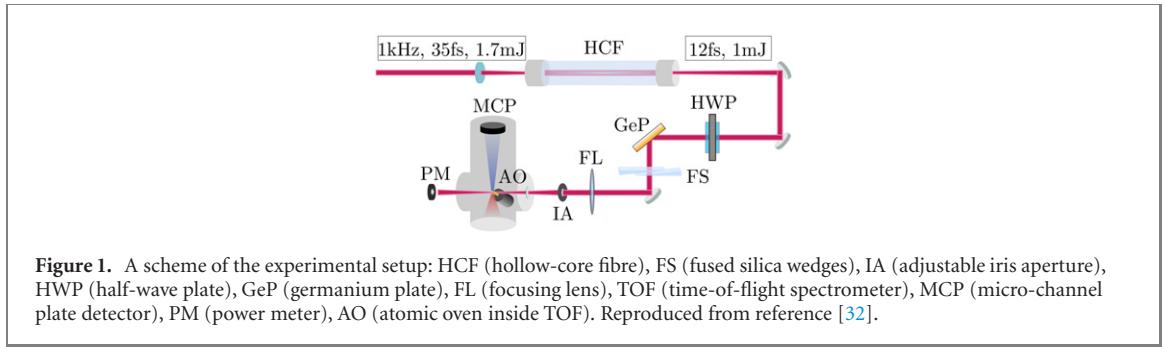
## 2. Theoretical background

The central result of this paper is the comparison and analysis of the rescattering efficiency of high-energy plateau electrons for four different alkali species. To reveal the origin of the significantly varying rescattering efficiencies, we numerically calculate electron-ion elastic differential scattering cross-sections (DCS). Details of the applied method can be found, e.g., in references [27–29]. Here, we give a short overview of the procedure.

Given is a spherically symmetric Coulomb-like potential $V = V(r)$. To model the alkalis in our calculations, we choose the semi-empirical pseudopotentials by Fuentealba [30]. The non-local, i.e., angular momentum quantum number $l$-dependent, character of these potentials can be expressed as [30]

$$V(r) = V_0(r) + \sum_l V_l(r)|l\rangle\langle l|, \qquad (1)$$

where $V_l(r)$ is an $l$-dependent short-range potential. Non-local potentials allow for a much more realistic description of the scattering process and have been found to be essential to accurately describe the laser-assisted scattering process is alkali metal atoms [24].

Next, the Schrödinger equation is solved under the assumption of an incoming particle with momentum $k = |\mathbf{k}|$, described by a plane wave scattering off $V$ and creating an outgoing spherical wave. Using the method of partial waves, an expression for the scattering amplitude $f(k, \theta)$ can be obtained [27], where $\theta$ is

**Figure 1.** A scheme of the experimental setup: HCF (hollow-core fibre), FS (fused silica wedges), IA (adjustable iris aperture), HWP (half-wave plate), GeP (germanium plate), FL (focusing lens), TOF (time-of-flight spectrometer), MCP (micro-channel plate detector), PM (power meter), AO (atomic oven inside TOF). Reproduced from reference [32].

the scattering angle. After calculating $f(k, \theta)$ by solving the radial Schrödinger equation for certain asymptotic boundary conditions, the DCS follows as

$$\frac{\mathrm{d}\sigma}{\mathrm{d}\Omega}(k, \theta) = |f(k, \theta)|^2. \tag{2}$$

This derivation is usually considered for short-range potentials. For Coulomb-like potentials the ansatz is similar and considers the superposition of a short-range potential with a Coulombic tail [28, 29].

Our numerical implementation of the described method is based on the openly available program 'elastic' [31]. The computation requires input parameters for the maximum, $l$, considered in the partial wave decomposition; the distance, $d$, after which the influence of the non-local short-range potential becomes negligible; and the size of the radial grid, $R$, used for the solution of the radial Schrödinger equation. All three variables were increased until the DCS became independent of the input parameters, guaranteeing convergence of the results.

## 3. Experimental setup

The experimental setup of this paper is shown in figure 1. A HE-TOPAS-C produces 50 fs laser pulses at a center wavelength of 1800 nm with 1 kHz repetition rate. This output is spectrally broadened inside an argon-filled hollow-core fiber, to obtain $(12 \pm 0.5)$ fs FWHMI few-cycle pulses with randomly varying CEP. The intensity of the radiation is controlled by changing the angle of the incoming linearly polarized light with respect to the s-polarization of a germanium plate's front surface, using a thin, motorized half-wave plate. After controlling the spectral phase using a pair of fused silica wedged, the beam is focused into a time-of-flight (TOF) spectrometer using a $CaF_2$ focusing lense ($f = 25$ cm). A power meter at the exit of the spectrometer tags the pulse energy of every single shot, allowing filtering of the data to remove long term laser fluctuations. The laser intensity is determined by a combination of pulse duration, power and focal spot size measurement; as well as a calibration by the $10U_p$ cutoff in xenon.

An atomic oven inside the TOF spectrometer is used to dispense the alkali-metal vapor into the interaction zone. It is heated to 270 °C, 216 °C, 178 °C and 159 °C for Na, K, Rb and Cs, respectively. At these temperatures, all dimer to monomer ratios, e.g. Na to $Na_2$, are well below 1%. Therefore, potential influences of the dimers on the photoelectron spectra (PES) can be neglected [33].

Independent of the results of this paper, and not shown here, a carrier-envelope phasemeter (CEPM) operated at 1800 nm was used to tag the CEP of every single laser shot in parallel to the experiment [26, 34]. By reducing the intensity to the multiphoton regime before each measurement, we can apply the method reported in reference [11]. Shortly, inclinations in the left-right emission asymmetry maps can be inspected to produce close to Fourier transform limited pulses in the interaction zone of the TOF spectrometer. This guarantees proper adjustment of the laser spectral phase by the use of the fused silica wedges.

## 4. Results and discussion

Before applying the concept of scaled interaction, we study the strong-field ionization of xenon at 1800 nm, a more well-known target at the shorter wavelengths [5, 35]. By combining the relatively high intensities with the sw-IR regime, we reach Keldysh parameters as low as $\gamma \approx 0.7$. CEP-averaged PES obtained with $(12 \pm 0.5)$ fs pulses at 1800 nm between $(2.5 \pm 0.4) \times 10^{13}$ W cm$^{-2}$ and $(6.0 \pm 0.9)10^{13}$ W cm$^{-2}$ are shown in figure 2.

The spectra exhibit the typical structures known from noble gas spectra at 800 nm. A sudden drop-off in yield near the $2U_p$ cutoff and a plateau structure reaching up to $10U_p$ [36]. However, clear differences to
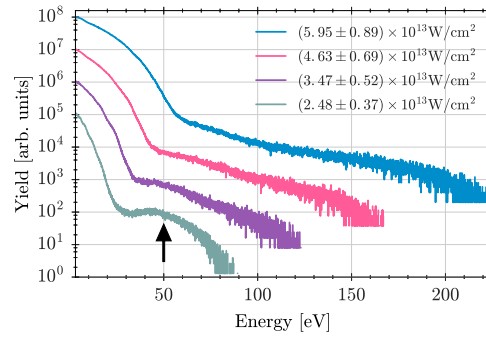
**Figure 2.** CEP-averaged PES of xenon at 1800 nm and $(2.5 \pm 0.4)$, $(3.5 \pm 0.5)$, $(4.6 \pm 0.7)$, $(6.0 \pm 0.9) \times 10^{13}$ W cm$^{-2}$ from bottom to top. Subsequent intensities are shifted upwards by one order of magnitude for better visibility. Reproduced from reference [32].

strong-field ionization of xenon at 800 nm are immediately observable. The height of the plateau region, as compared to the direct-electron portion of the spectrum, is much lower than at the shorter wavelengths, e.g., see figure 1 in reference [26]. Moreover, the 'bump' in the plateau of xenon at 800 nm [5] is only recognizable at the lowest intensity, see arrow in figure 2.

Next, we present CEP-averaged measurements of intensity-resolved ATI spectra for sodium to caesium, ionized by $(12 \pm 0.5)$ fs radiation at 1800 nm, in figure 3. The figure contains selected spectra for intensities between $(0.5 \pm 0.1) \times 10^{13}$ W cm$^{-2}$ and $(1.4 \pm 0.2) \times 10^{13}$ W cm$^{-2}$. Since alkali atoms have a lower ionization potential as compared to xenon, the intensity was reduced to avoid significant depletion of the atoms. At the highest intensity, the Keldysh parameters are between $\gamma \approx 0.8$ and $0.7$. This places the results of this section into the tunneling regime.

Immediately noticeable in figure 3 is the strong similarity between the strong-field ionization of potassium and rubidium (second and third panel). The $2U_p$ cutoff can be observed as a dent between 5 eV and 8 eV. This dent is more pronounced in potassium, but also noticeable in rubidium, see black arrow in figure 3. The typical horizontal plateau structure appears more elevated in these two species.

In contrast, sodium (figure 3 top panel) shows a distinct horizontal plateau reaching from $\approx 4$ to $10U_p$. However, despite its clear optical visibility, the yield in the plateau region between 30 eV and 40 eV lies 3.5 to 4 orders of magnitude below the direct electrons. Potassium and rubidium, on the other hand, fall off by 2.5 to 3 orders of magnitude only.

Caesium spectra (figure 3 bottom panel) display a combination of the structures of the previous alkalis. A small dent towards the end of the direct electron energy region is visible below 10 eV, whereas the high-energy electrons decay in the same arching manner as potassium and rubidium. The yield in the high-energy region, as compared to the direct electrons, is stronger than in sodium, but lower than in potassium and rubidium. Namely, it is 3 order of magnitude below the direct electrons. Moreover, at the two highest intensities, we recognize a distinguishable, horizontal plateau structure emerging at very high electron energies. Equally interesting is the observation that Cs has much more pronounced ATI peaks at the lower intensities than the other alkalis. So far, we are unable to explain these two observations, which warrant further investigation.

We now turn to the main results of this paper, the quantitative evaluation of different alkali species with respect to their rescattering efficiency. As noted, the rescattering process plays a fundamental role in light–matter interaction. Further, efficient rescattering of the emitted electron on the parent ion is a necessity for certain applications, e.g., the CEPM.

To this end, we analyse intensity-resolved measurements of the 12 fs short-pulse CEP-averaged ATI spectra, as they are shown in figure 3. Note that this figure only displays selected intensities. More intensities were recorded during the measurement.

To determine the rescattering efficiency of the different alkalis, we divide their ATI spectra into three energy regions: $0–2.5U_p$; $2.5–6U_p$ and $>6U_p$. These are typical energy regions for direct, medium- and high-energy electrons as given by the three-step model [37]. For each intensity, the yield in each region is integrated and normalized to the total ionization yield, i.e., the integral over the entire spectrum. The result is shown in figure 4.

For further comparison, figure 4 also contains the same analysis for xenon at 1800 nm and 12 fs. As xenon's $I_p$ is much higher, its ionization was performed at higher intensities. The upper $x$-axis in panels (a)–(c) of figure 4 refers to the intensity axis of the xenon data. With the experimental setup, the highest achievable intensity was $(6.0 \pm 0.7) \times 10^{13}$ W cm$^{-2}$.
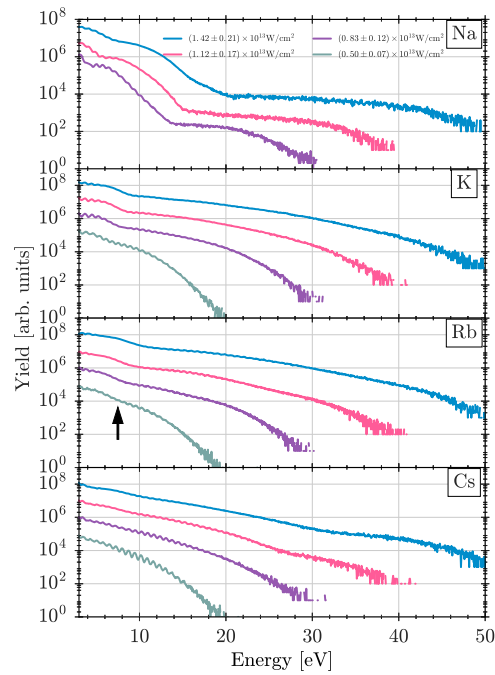
**Figure 3.** CEP-averaged PES of alkali metal atoms at 1800 nm and $(0.5 \pm 0.1) \times 10^{13}$ W cm$^{-2}$ (green), $(0.8 \pm 0.1) \times 10^{13}$ W cm$^{-2}$ (purple), $(1.1 \pm 0.2) \times 10^{13}$ W cm$^{-2}$ (pink) and $(1.4 \pm 0.2) \times 10^{13}$ W cm$^{-2}$ (blue), from bottom to top. For sodium, the lowest intensity was not measured due to very low count rate. For better visibility, each subsequent intensity it shifted upwards by one order of magnitude. Same colors were measured at the same intensity. Reproduced from reference [32].

In regards to the question of rescattering efficiency, figure 4(c) is the most significant. Here, we find quantitative confirmation of the qualitative observations we made on the intensity-resolved ATI spectra in figure 3. Namely, the rescattered electron yield of sodium is about one order of magnitude lower than caesium and even two orders of magnitude below rubidium and potassium. For different laser parameters, a similar conclusion about the low rescattering efficiency of sodium was drawn in reference [24]. This presents a remarkable result. In a simplistic picture, one would assume the rescattering efficiency to increase, as the size of the parent ion and therefore the rescattering center increases, i.e., caesium should create the most rescattered electrons.

We identify potassium as the most efficient rescatterer in the parameter regime investigated by us. It is followed very closely by rubidium. Caesium is about one order of magnitude lower than the two aforementioned alkalis. Importantly, these three species display a higher rescattered yield than xenon, despite xenon's known large DCS in the backscattering regime at 800 nm [27]. This is due to the fact that ionization of xenon was performed at four times the intensity of the alkalis. Therefore, the maximum impact energy ($\propto 3.2U_{\mathrm{p}}$) in xenon is four times higher as well. Decreasing the intensity for xenon is not a practical option, as the count rate would significantly decrease. Therefore, in this parameter regime, alkali-metal atoms are indeed an advantageous candidate over xenon, if a high flux of high-energy rescattered electrons is required.

Panel (b) of figure 4 shows that the qualitative trends for electrons with energies between 2.5 and $6U_{\mathrm{p}}$ are similar to the high-energy region. The differences in orders of magnitudes are not as severe as before, around one or less. However, in this region sodium displays a higher yield than xenon. Panel (a) reveals where the 'missing' high-energy yield in sodium is located. Of all alkalis, it has the largest relative amount of low-energy direct electrons.

Next, we want to reveal why figure 4(c) exhibits the discussed behavior. The answer is found in panel (d), where we show backscattering DCSs ($\theta = 180°$) for sodium to caesium at the relevant return energies. The upper *x*-axis indicates the required intensity, such that the $3.2U_{\mathrm{p}}$ cutoff corresponds to the lower *x*-axis' impact energy at 1800 nm.

Astonishingly, the simple evaluation of the DCSs at the maximum return energy captures most of the details of figure 4(c). Panel (c) shows that, at $1.0 \times 10^{13}$ W cm$^{-2}$, rescattering in rubidium/potassium is about 2 orders of magnitude stronger than in sodium. Comparison with the DCSs at the corresponding $3.2U_{\mathrm{p}}$ impact energy yields 1.2 orders of magnitude. However, if we considering the product of the ionization rate with the volume of the isointensity spheres inside the focus, we find that ionization predominantly occurs at $0.7 \times 10^{13}$ W cm$^{-2}$. Here, we read off 1.6 orders of magnitude difference from the
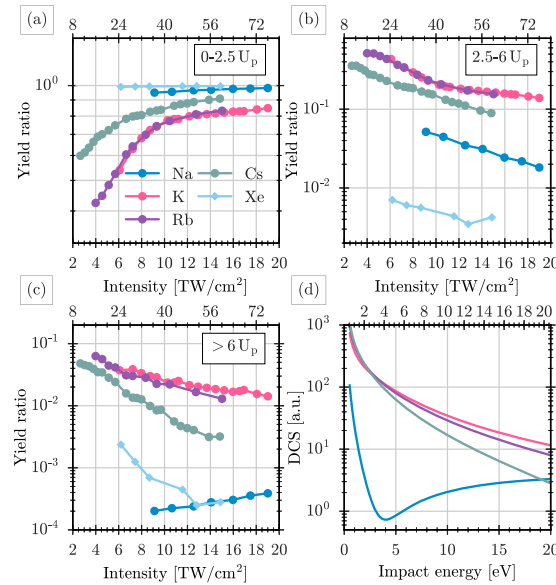
**Figure 4.** Measured rescattering efficiency of sodium to caesium and xenon at 1800 nm. The panels show the integrated yield in three energy regions $0-2.5U_p$ (a); $2.5-6U_p$ (b); and $>6U_p$ (c); normalized to the total yield. The upper *x*-axis refers to the intensity of the xenon measurement. Panel (d) illustrates the impact energy dependent backscattering DCS for sodium to caesium. The upper *x*-axis refers to the intensity required, such that the $3.2U_p$ cutoff corresponds to the impact energy at 1800 nm. The DCS are in good agreement with the results of panel (c). The legend is identical in all panels. Reproduced from reference [32].

DCSs, which is closer to the measured value. The remaining difference can be explained by the existence of electrons with lower return energies.

Potassium and rubidium are almost similar in their rescattering behavior. However, as the intensity is increased, potassium develops a slightly larger rescattering efficiency than rubidium in the measurement. This behavior is exactly reflected by the DCSs. While this small effect is interesting to note, it may be a coincidence and is not within the measurement's accuracy.

The rescattered yield in the high-energy region decreases for all alkalis, as the intensity is increased. Only sodium behaves contrary to this trend. The DCSs in figure 4(d) confirm this behavior as well. For return energies higher than 4 eV, sodium's DCS predicts an increase in backscattered electrons, whereas for all other alkalis, this probability decreases. This is in agreement with the measured data in figure 4(c). The analysis shows that most of the effects regarding the yield of rescattered electrons in alkalis can be traced back to their respective DCSs. Similar conclusions were drawn for the noble gases around 800 nm [27, 38].

Next, we wish to gain a deeper physical understanding of the origin of the species-dependent DCSs. In reference [24], it was found that the strong rescattering in potassium originates from the attractive *d* channel of its atomic potential. If this channel is exchanged with the hydrogenic *d* channel in a time-dependent Schrödinger equation calculation, the plateau region in potassium decreases by almost two orders of magnitude. We perform a similar analysis by plotting the sum of $V_0$, $V_d$ and the centrifugal term, see equation (1), in figure 5. We observe that the depth of the potential well, i.e., its global minimum, adheres to the same sequence as the rescattering efficiencies. Namely, Potassium exhibits the deepest well, followed by rubidium. Sodium's exceptionally low DCS further follows from its repulsive *d* channel, in stark contrast to the other alkalis. Therefore, we conclude that the properties of the respective atomic potential *d* channels are mainly responsible for the differences in the DCSs for the alkalis under discussion.

Note that the species-dependent strength of the plateau for noble gases has previously been studied [5]. While differences for the species from helium to xenon certainly exist, the sensitivity of the plateau in alkali-metal atoms to the target is much more pronounced. This gives further evidence to the claim that SFI can show significant differences even for atomic targets with similar $I_p$. A fact, which is not considered by the concept of scaled interaction.

The aforementioned dynamics also give rise to the practical application of measuring the CEP in the sw-IR. An apparatus called the carrier-envelope phasemeter (CEPM) [25] can exploit a significant yield of rescattered plateau electrons to measure the CEP of single lasers shots up to several 100 kHz [39]. The technology is well established at 800 nm and could recently be extended to 1800 nm using xenon as a target gas [26]. However, various challenges present themselves at the longer wavelength, which only become more critical in the MIR regime. A potential solution of these challenges is the step to a low-$I_p$ target, with alkalis
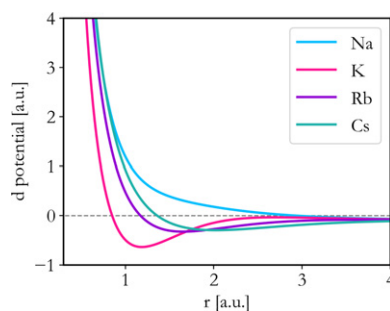
**Figure 5.** The $d$ potential, i.e., sum of $V_0$, $V_d$ and centrifugal term, for the four investigated alkalis. The depth of the potential well is the main contributing factor of the species-dependent DCSs.

being a prime candidate. We have presented evidence that such a phasemeter should rely on potassium or rubidium to produce the best signal to noise ratio during the CEP measurement. This might be an important tool for future studies in the sw-IR/MIR regime as control over the CEP has been shown to be crucial for the generation of isolated attosecond pulses [40, 41].

## 5. Summary

In summary, we have measured the intensity-dependent rescattering efficiency of four different low-$I_p$ alkali targets. Significant differences in the species-dependent alkali ATI spectra could be observed. Specifically, the height of the plateau is most pronounced in potassium. This effect could be traced back to be a direct consequence of the electron-ion differential scattering cross section. Pairing the low ionization potential of these atoms with longer wavelengths allows us to effectively scale the interaction to match the ionization regime of the more well-known nobel gas spectra in the visible. Thereby, reproducing some of the typical features in the alkali ATI spectra, e.g., the direct electron cutoff and rescattered election plateau. However, the low-$I_p$ targets show additional, and so far unexplained, effects, for example in Cs we observe both enhanced ATI peaks at low intensities and a secondary plateau that only emerges at high intensities and large electron energies. Finally, knowledge of the rescattering efficiency is crucial for predicting the relative strength of the ATI plateau. Consequently, this allows one to scale the interaction to allow for a CEPM at lower intensities in the sw-IR/MIR regime.

## Acknowledgments

## Reference

[1] Agostini P, Fabre F, Mainfray G, Petite G and Rahman N K 1979 Free-free transitions following six-photon ionization of xenon atoms *Phys. Rev. Lett.* **42** 1127−30

[2] Ferray M, L'Huillier A, Li X F, Lompre L A, Mainfray G and Manus C 1988 Multiple-harmonic conversion of 1064 nm radiation in rare gases *J. Phys. B: At. Mol. Opt. Phys.* **21** L31

[3] L'Huillier A, Lompre L A, Mainfray G and Manus C 1983 Multiply charged ions induced by multiphoton absorption in rare gases at 0.53 $\mu$m *Phys. Rev.* A **27** 2503−12

[4] Keldysh L V 1965 Ionization in the field of a strong electromagnetic wave *Sov. Phys. JETP* **20** 1307

[5] Paulus G G, Nicklich W, Xu H, Lambropoulos P and Walther H 1994 Plateau in above threshold ionization spectra *Phys. Rev. Lett.* **72** 2851−4

[6] Popmintchev T *et al* 2012 Bright coherent ultrahigh harmonics in the kev x-ray regime from mid-infrared femtosecond lasers *Science* **336** 1287−91

[7] Silva F, Teichmann S M, Cousin S L, Hemmer M and Biegert J 2015 Spatiotemporal isolation of attosecond soft x-ray pulses in the water window *Nat. Commun.* **6** 6611

[8] Colosimo P *et al* 2008 Scaling strong-field interactions towards the classical limit *Nat. Phys.* **4** 386−9

[9] Tate J, Auguste T, Muller H G, Salières P, Agostini P and DiMauro L F 2007 Scaling of wave-packet dynamics in an intense midinfrared field *Phys. Rev. Lett.* **98** 013901

[10] Shiner A D *et al* 2009 Wavelength scaling of high harmonic generation efficiency *Phys. Rev. Lett.* **103** 073902

[11] Zille D, Adolph D, Möller M, Sayler A M and Paulus G G 2018 Chirp and carrier-envelope-phase effects in the multiphoton regime: measurements and analytical modeling of strong-field ionization of sodium *New J. Phys.* **20** 063018

[12] Fuest H *et al* 2019 Diffractive imaging of $c_{60}$ structural deformations induced by intense femtosecond midinfrared laser fields *Phys. Rev. Lett.* **122** 053002

[13] Lai Y H, Blaga C I, Xu J, Fuest H, Rupp P, Kling M F, Agostini P and DiMauro L F 2018 Polarizability effect in strong-field ionization: quenching of the low-energy structure in $c_{60}$ *Phys. Rev.* A **98** 063427

[14] Johannes P *et al* 2017 Nanoplasmonic electron acceleration by attosecond-controlled forward rescattering in silver clusters *Nat. Commun.* **8** 1181

[15] Schütte B *et al* 2018 Low-energy electron emission in the strong-field ionization of rare gas clusters *Phys. Rev. Lett.* **121** 063202

[16] Park D J, Piglosiewicz B, Schmidt S, Kollmann H, Mascheck M and Lienau C 2012 Strong field acceleration and steering of ultrafast electron pulses from a sharp metallic nanotip *Phys. Rev. Lett.* **109** 244803

[17] Wessels P, Ruff B, Kroker T, Kazansky A K, Kabachnik N M, Sengstock K, Drescher M and Simonet J 2018 Absolute strong-field ionization probabilities of ultracold rubidium atoms *Commun. Phys.* **1** 32

[18] Schuricke M *et al* 2011 Strong-field ionization of lithium *Phys. Rev.* A **83** 023413

[19] Morishita T and Lin C D 2013 Photoelectron spectra and high rydberg states of lithium generated by intense lasers in the over-the-barrier ionization regime *Phys. Rev.* A **87** 063405

[20] Schuricke M, Bartschat K, Grum-Grzhimailo A N, Zhu G, Steinmann J, Moshammer R, Ullrich J and Dorn A 2013 Coherence in multistate resonance-enhanced four-photon ionization of lithium atoms *Phys. Rev.* A **88** 023427

[21] Gallagher T F 1994 *Rydberg Atoms, Cambridge Monographs on Atomic, Molecular and Chemical Physics* (Cambridge: Cambridge University Press)

[22] Maeda H, Gurian J H and Gallagher T F 2011 Population transfer in the na s-p rydberg ladder by a chirped microwave pulse *Phys. Rev.* A **84** 063421

[23] Park H, Tanner P J, Claessens B J, Shuman E S and Gallagher T F 2011 Dipole-dipole broadening of rb *ns − np* microwave transitions *Phys. Rev.* A **84** 022704

[24] Gaarde M B, Schafer K J, Kulander K C, Sheehy B, Kim D and DiMauro L F 2000 Strong species dependence of high order photoelectron production in alkali metal atoms *Phys. Rev. Lett.* **84** 2822−5

[25] Rathje T *et al* 2012 Review of attosecond resolved measurement and control via carrier−envelope phase tagging with above-threshold ionization *J. Phys. B: At. Mol. Opt. Phys.* **45** 074003

[26] Zhang Y *et al* 2017 Single-shot, real-time carrier-envelope phase measurement and tagging based on stereographic above-threshold ionization at short-wave infrared wavelengths *Opt. Lett.* **42** 5150−3

[27] Čerkić A, Hasović E, Milošević D B and Becker W 2009 High-order above-threshold ionization beyond the first-order born approximation *Phys. Rev.* A **79** 033413

[28] Joachain C J 1979 *Quantum Collision Theory* (Amsterdam: North-Holland)

[29] Schiff L I 1968 *Quantum Mechanics* (New York: McGraw-Hill)

[30] Fuentealba P 1982 On the reliability of semiempirical pseudopotentials: dipole polarisability of the alkali atoms *J. Phys. B: At. Mol. Phys.* **15** L555

[31] Schultz D R and Reinhold C O 1998 Elastic−elastic scattering of electrons from ions and atoms *Comput. Phys. Commun.* **114** 342−55

[32] Zille D 2018 Scaling ultrashort light−matter-interaction to the short-wave infrared regime and beyond *PhD Thesis* Friedrich-Schiller-University Jena

[33] Singh J 2010 Alkali-hybrid spin-exchange optically-pumped polarized $^3$He targets used for studying neutron structure *PhD Thesis* University of Virginia

[34] Wittmann T, Horvath B, Helml W, Schatzel M G, Gu X, Cavalieri A L, Paulus G G and Kienberger R 2009 Single-shot carrier-envelope phase measurement of few-cycle laser pulses *Nat. Phys.* **5** 357−62

[35] Yang B, Schafer K J, Walker B, Kulander K C, Agostini P and DiMauro L F 1993 Intensity-dependent scattering rings in high order above-threshold ionization *Phys. Rev. Lett.* **71** 3770−3

[36] Paulus G G, Becker W, Nicklich W and Walther H 1994 Rescattering effects in above-threshold ionization: a classical model *J. Phys. B: At. Mol. Opt. Phys.* **27** L703

[37] Corkum P B 1993 Plasma perspective on strong-field multiphoton ionization *Phys. Rev. Lett.* **71**

[38] Walker B, Sheehy B, Kulander K C and DiMauro L F 1996 Elastic rescattering in the strong field tunneling limit *Phys. Rev. Lett.* **77** 5031−4

[39] Hoff D, Furch F J, Witting T, Rühle K, Adolph D, Max Sayler A, Vrakking M J J, Paulus G G and Schulz C P 2018 Continuous every-single-shot carrier-envelope phase measurement and control at 100 khz *Opt. Lett.* **43** 3850−3

[40] Goulielmakis E *et al* 2008 Single-cycle nonlinear optics *Science* **320** 1614−7

[41] Sansone G *et al* 2006 Isolated single-cycle attosecond pulses *Science* **314** 443−6